



Review on Processing and Fluid Transport in Porous Metals with a Focus on Bottleneck Structures

A. J. Otaru¹

Received: 13 June 2019 / Accepted: 26 June 2019 / Published online: 13 July 2019
© The Korean Institute of Metals and Materials 2019

Abstract

The dynamics of fluid in porous metals has earned growing attention due to the increasing worldwide research and technological advancement in harnessing, processing and the use of materials. In this study, a review on the wide range of different structures that metal foams can show, the range of processing methods that can be used to make them, leading to these different structures and their fluid flow behaviour are presented herein. The fluid section of this investigation covers fluid flow models, boundary conditions, permeability and Form drag estimations, Reynolds number and friction factor determinations, state-of-the-art knowledge of experimental and predictive results. It is the hope that the extended review on processing and fluid flow across monomodal “bottleneck” metallic structures covered herein would lend itself useful to the processing of enhanced bimodal “bottleneck” structures for fluid flow application.

Keywords Metal foams · Processing · Fluid flow

1 Introduction

Metal foam is a near-net or sponge-like shape cellular structure consisting of a solid matrix (also termed as skeletal configurations or “struts”), visual fascinating pores and pore openings. Porous metallic structures can be made from any metallic materials like aluminium, titanium, nickel, steel, copper, nickel, chromium and metal alloys. They are generally classified into close-celled (air-sealed) or open-celled (interconnecting pores) as shown by the micrographs in Fig. 1. Unlike packed beds, porous metallic structures are characterized by high porosity typically, between 75 and 95% (air-filled) and pore sizes between 0.2 and 5.0 mm which signify their defining characteristics of high surface area and ultralight materials and enabling their usefulness for high pressure, load bearing and high-temperature applications [1–3]. If metal can be made pressed or sintered, there is every possibility that it could be made porous and the resulting effect is a change in its microstructure [4] to produce open-celled foams.

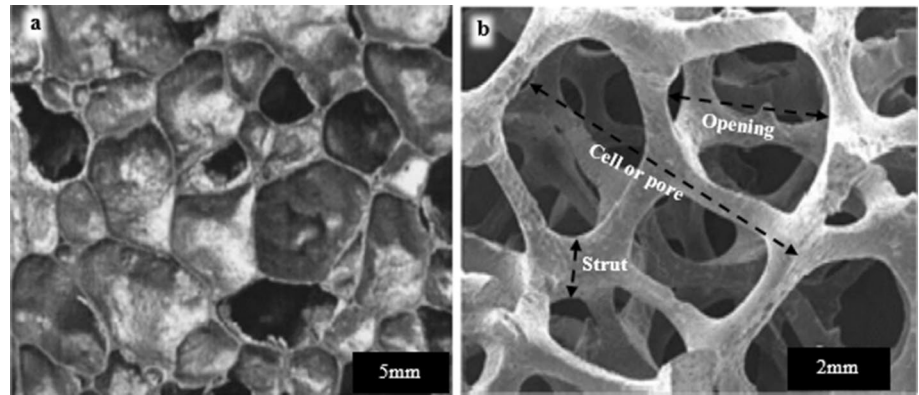
The interconnecting pores or pore openings in porous metallic structures are generally considered as an open volume within the matrix network that allows the uniform length of passages and distribution [6]. The consideration of these pore openings during metallic foam manufacturing process is largely dependent on their applications. Examples of these applications include filters for high-temperature gas and fluid filtration [7], energy absorbers/package and heat exchanger [8], acoustics and vibrational control [9], catalytic supports [10], biomedical devices [11], lightweight structure and mechanical damping [12].

Understanding the behaviour of fluid permeation through porous metallic structures is quite important in the design and optimization of enhanced porous materials for the process. Unlike flow through packed beds where the permeation of fluid is mainly dictated by their void spaces (interstices), flow through open-celled metallic foams as described in [13] to rendered more complex by the opening of their interconnecting pores or “windows”. This interconnection in porous metallic structures enables their high porosity, permeability, high specific surface (defined as the ratio of foam surface area per unit bulk volume) [14, 15]. These unique attributes of porous metals enable their wide range of applications involving pressure drops (fluid flow) and have seen them chosen over packed beds. In this review, we look to explore the different types of porous metallic structure,

✉ A. J. Otaru
otaru_12257@yahoo.com

¹ Department of Chemical Engineering, Federal University of Technology, P.M.B. 065, Gidan-Kwanu, Bida Road, Minna, Nigeria

Fig. 1 Micrographs of **a** close-celled and **b** open-celled porous metallic structures Sourced, Ref. [5]



manufacturing processes and their fluid flow application as given in the ensuing sections respectively with a focus on low-pore volume porous metallic structures.

2 Metal Foam Processing

Cellular metals are categorized into different type largely dependent on their manufacturing routes leading to their differences in structural morphology and porosity of the materials. Commercially available porous metallic sponges like Recemat™, (Dodewaard, the Netherland), Incofoam now, Alantum™ (Seongnam-city, Korea), Duocel™ (ERG, Oakland, CA, USA) are classified as highly-porous structure characterised by pore volume fractions between 80 and 95% and can be produced by replication of an open-celled porous polymeric structures [16]. The structural morphology of these structures are characterised by an obvious pore network similar to the topology of synthetic fibre materials like polyurethane and polyethylene. Their production methods are quite advanced aided by uniform pore networks and distribution and making them suitable for light-weight engineering applications. However, their excessive production steps often increase production costs and has limited manufacturer to consider other technological routes. Other manufacturing routes for the processing of porous metallic structures are powder-technology (Alulight) or melt processes (Hydro/Alcan, Alporas, Formgrip/Foamcast, and Gasar) [17, 18]. All these processes mentioned have their shortcomings in either the achievement of highly irregular or sponge-like structures with wide pore-size distribution or limited levels of porosity. Images of these foams indicating the structural morphology (pore sizes and openings) are presented in Fig. 2.

2.1 Hydro/Alcan

The Hydro/Alcan also termed as direct-foaming involves the production of foam by gas injection of liquid melts [19]. The

first step in the process is the preparation of aluminium melt followed by the enhancement of the melt viscosity with the addition of either carbide, aluminium-oxide or magnesium oxide particles. Various alloys of aluminium can be used for this process, but care should be taken to ensure uniform distribution of the viscosity enhancement particles. Rotating impeller or vibrating nozzles are used to inject gases (air, nitrogen, argon) into the melt and consequently generates uniform bubbles in the melt. The presence of particles in the melts makes the foam relatively stable and can be pulled off the liquid surface with the help of conveyor belts. Upon cooling and solidification, the resulting composite is a low-volume near-net shaped metal matrix as shown by Fig. 2a [20]. This direct-foaming process has the advantages of continuous production of large volume of porous metallic structures and reduced production costs than other types of porous metals. A possible disadvantage of this direct-foaming is the limited level of achievable densities, typically, between 0.069 and 0.54 g/cm³ resulting in low level of pore fluid volume fraction. The eventual necessity for cutting the foam could result in the further cell openings and alteration of the pore networks. The average pore sizes of the resulting porous metals made by this route range between 25 mm down to 3 mm whilst the wall thickness ranges between 50 and 85 mm. Such cellular structures are characterised by high surface area enabling their suitability for heat transfer and load-bearing applications.

2.2 Alporas

Unlike the Hydro/Alcan foam produced by the gas injection process, the Alporas type of porous metallic structure is produced by the addition of blowing agents to the melt [21]. The first step in this process is the addition of calcium metal to an aluminium melt (680 °C). The presence of this calcium metal increases the viscosity of the melt upon stirring and at this extreme operating temperature, calcium oxide (CaO), calcium aluminium oxide (CaAl₂O₄) are formed. After achieving the desired melt viscosity

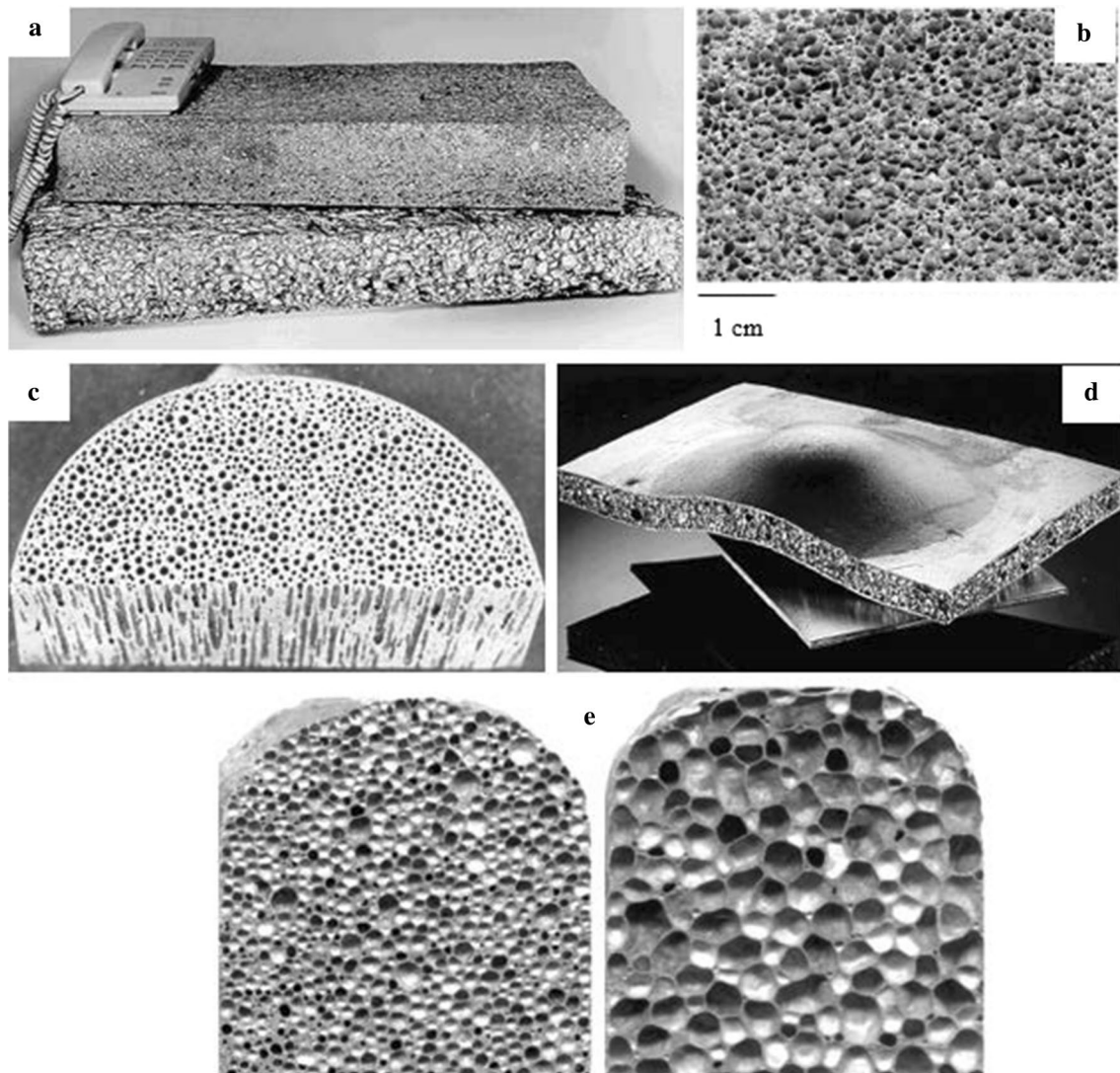


Fig. 2 Samples of porous metallic foam structures made by **a** foaming of melts by gas injection (Hydro/Alcan) (sourced from [20]). **b** Foaming of melts with blowing agents (Alporas) (sourced from [22]). **c** Solid–Gas eutectic solidification (Gasar) characterized by largely elongated pore structures (sourced from [23]). **d** Foaming of pow-

der compacts (Foaminal/Alulight), steel/aluminium foam/steel sandwich (sourced from [24]) and **e** Two samples of aluminium/silicon carbide foam made by Foaming of ingots containing blowing agents (Formgrip/Foamcast) (sourced from [25])

(usually increasing by a factor of up to five), 1.6 wt% titanium oxide (TiH_2) is added as the blowing agent which releases hydrogen gas into the liquid melt. At constant pressure, the melt gradually expands and fills the vessel and upon cooling, the liquid melt turns into a solid porous metallic sponge as shown in Fig. 2b [22]. This foam making route has the advantage of achieving structural homogeneity resulting in an empirical relation between melt viscosity and cell diameter and between melt viscosity and final foam density. Though, accurate control of technological parameters is reportedly [22] difficult aided by complicated mechanical agitation and temperature cycle.

2.3 Gasar

The Gasar type of porous metallic structure is formed by solid–gas eutectic solidification process. The word “Gasar” refers to gas-reinforcement and particularly describes porous metallic structure made by solid–gas eutectic solidification [21, 26]. This approach exploits the fact that a homogeneous melt charge with hydrogen can be achieved by the melting of metals in a hydrogen atmosphere at an extremely high pressure typically, up to 50 atm. At low temperature, a heterogeneous two-phase system is formed because of the eutectic transition of the melt. The topology (geometrical

representation) of this material is largely controlled by the hydrogen content, chemical composition of the melt, the rate of heat removed and pressure over the liquid melt. Figure 2c presents the image of Gasar foam structure characterized by obvious non-uniform pore-size distribution resulting from coalescence and the concurrent growth of small (10 μm diameter) to large (10 mm diameter) pores within the metal matrix. This technological route of foam making has the advantage of producing low-porosity porous metals (5–75%) suitable for high impact and load-bearing applications but the lack of accurate control of pore size network within the metal matrix remains a possible setback.

2.4 Foaminal/Alulight

The Foaminal/Alulight foam is made via foaming of powder compacts [24]. The manufacturing process begins with the embodiment of blowing agents into metal powder (aluminium, zinc, brass, tin, gold, lead, and alloys) followed by compaction to yield a dense nearly-finished product. The metal powders could be in the form of alloy powders or elementary metal powders. Rod-extrusion, or powder rolling, isostatic or uniaxial compression are known compaction methods adopted in this technological route of foam processing. Secondly, heat treatment at an extremely high temperature (near the melting point of porous materials) helps to decompose the evenly distributed blowing agents thereby releasing gas and forces the melt to expand significantly. Though, the extent of the melt expansion is largely dependent on the melting temperature and precursor size from a few seconds to several minutes. Figure 2d presents a highly porous “Alulight” aluminium foam sandwiched between two metal face sheets bonded together with an adhesive [24]. This foaming route has the advantage of producing a highly porous cellular core with closed outer skin suitable for light-weight and energy absorption applications. However, small-scale commercial production of porous metals by this route currently exist due to the difficulty in accurate control of the melt expansion during heat treatment. If the expansion is not limited, the resulting metal matrices are reported [24] to having undefined shapes.

2.5 Formgrip/Foamcast

The term Formgrip/Foamcast is an acronym for reinforced metals by gas release in precursor [27]. This type of porous metallic structures is made by foaming of Ingots containing blowing agents. The term Ingot refers to metal typically oblong in shape. Unlike the metal powder compaction process, this type of foam is made by the modification of powder-compact melting process through the homogeneous addition of TiH_2 particles into an aluminium melt. In this case, the melt is quickly cooled down below the melting

point of the material after mixing to avoid premature hydrogen evolution. The delay in the decomposition of the earlier routes (Alulight) is attributable to the fact that an oxide barrier is formed on each particle of TiH_2 resulting from the heat treatment process [24]. Figure 2e present images of porous metallic structures made by the Formgrip process. The Formgrip enables the production of cellular metals with a variety of different pore networks largely attributed to the challenging homogeneous distribution of TiH_2 particles in a die-casting machine.

2.6 Replication Casting Route Using Space Fillers

Controlling the pore-volume and sizes of metal foams is crucial during manufacturing processes. The best and most economical way to this problem will be incorporating a volume of sacrificial space fillers [4]. This is a manufacturing route in which a liquid metal (material) is poured into a metallic vessel consisting of hollow spheres of the desired shape and then allowed to solidify after mixing before compaction. The porous hollow sphere is removed by dissolution in warm water or thermal degradation to leave porosity [28, 29]. The step by step approaches to the processing of this unique structure adopting the replication method is represented in Fig. 3.

This replication process of manufacturing light-weight porous metal foams for engineering applications described in [4] can be done by casting liquid metals around organic or inorganic hollow spheres (packed beds of salts or porogens) of low density or by introducing this sphere into a metallic melt. Inorganic fillers materials are fired clay pellets loose sand pellets, foamed glass sphere, loose bulks of expanded clay granules [31] while polymer spheres are classified as organic space fillers and can be used as space holder if the solidification of the melt is sufficiently fast [32]. Continuous pores are connected with touching spheres to allow the flow of fluid from one side to another. The resulting interconnection of these pores has overall effects on the structural-related parameters and the overall flow behaviour (pressure drop) of the porous medium. Typical examples of these structural-related parameters of porous metallic structures are porosity, tortuosity, pore volume, pore sizes, pore openings and surface area [9, 33]. Preheating of the bulk of space holders is employed during metal foams processing to avoid premature solidification of the melt especially at low infiltration pressure or high heat capacity of the material [32].

The space holding or replication casting route has the advantage that the morphology of the pore sizes can be manipulated through the sizes of the space holders (salts or porogens) and has overall effects on the foam porosity by controlling porogens packing density. The sizes of the pore openings within the metal matrix made by this replication route are largely dependent on the applied differential

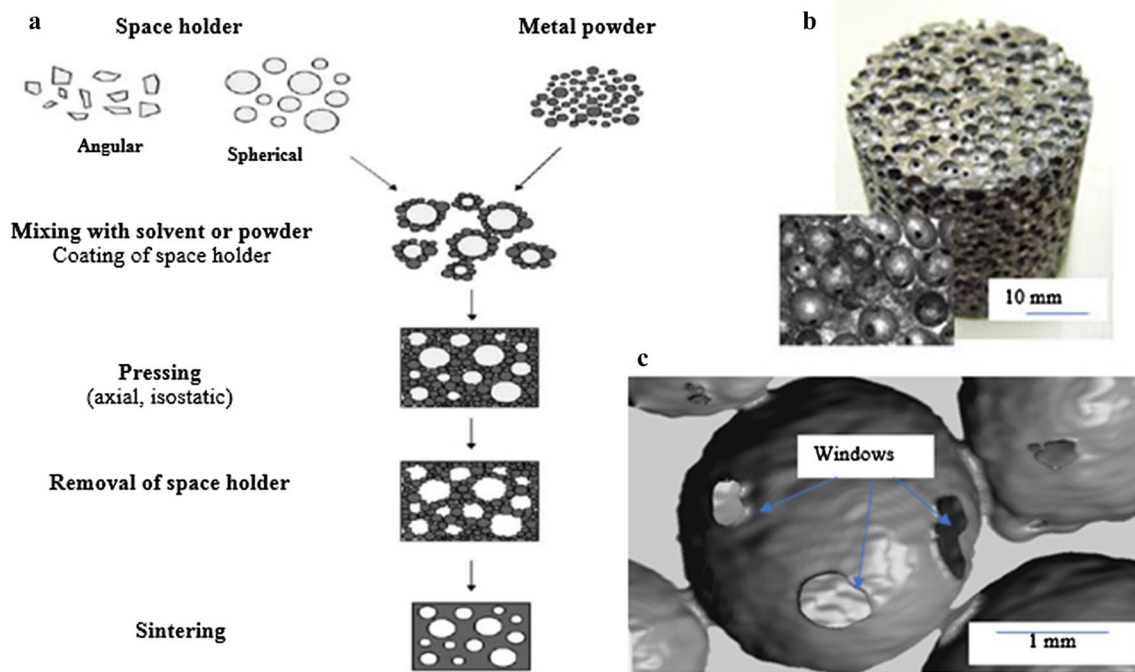


Fig. 3 **a** Left is the space-holding routes of metal foams production (sourced from [29]), **b** to the top right is an optical micrograph of porous metal made by replication casting of near-spherical packed

beds of salts and **c** to the bottom right is a tomography image showing the typical pore sizes and pore openings (sourced from [9, 30])

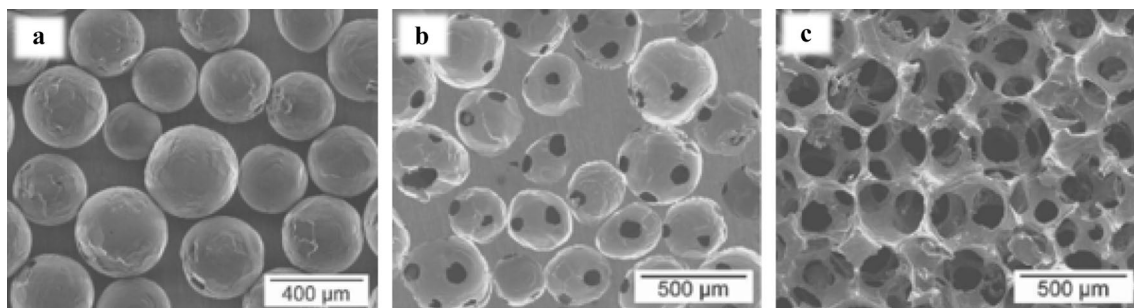


Fig. 4 **a** Scanning electron microscopy (SEM) images of 400 µm diameter NaCl beads and right, are porous aluminium structures with bottleneck pore networks of mean pore diameter size of 400 µm and fluid volume fraction of **b** 0.69 and **c** 0.90. Sourced from [39]

pressure used to drive the liquid melts into the convergent gaps created by the hollow spheres [4, 30, 33]. Thus, larger pore openings signify lower applied differential pressures, conversely, smaller openings indicate the presence of high applied differential pressures which forces the liquid melts into the spaces created by the porogens. Such porous metallic structures made by this replication casting of spherical beds are reportedly [9, 30, 33–37] known as “bottleneck” structures. Figure 4 presents scanning electron microscopy (SEM) images of 400 µm diameter spherical NaCl salts and “bottleneck-type” porous aluminium structures made by the space holding technique of similar pore diameter sizes but different pore fluid volume fractions and pore openings [37]

largely influenced by the spheres packing density and depth of infiltration of the liquid melts into the convergent gap created by the packed beds respectively. Similar replication casting route was reported in [33] in the production of “bottleneck-type” porous aluminium of similar pore sizes and different connectivity presented by Fig. 5 whilst Fig. 6 presents porous aluminium structures made by the same technological route but separated by different pore diameters sizes [34] largely influenced by the sizes of the salt beads used.

The pore connectivity of these structures also termed as “window sizes” connecting two spheres within the porous matrix was considered in [38] to be a function of pore radii (r_p) and the degree of infiltration of liquid melts into the

Fig. 5 X-ray computed tomography of 2D processed model contour and 3D representative volume element (RVE) of the solid phases of “bottleneck-type” porous aluminium structures made by replication process of applied differential pressure, pore fluid volume fraction, mean pore diameter size and mean pore connectivity of **a** 1 bar, 0.71, 2.23 mm and 0.69 mm, **b** 0.25 bar, 0.78, 2.23 mm and 0.90 mm respectively. Sourced from [33]

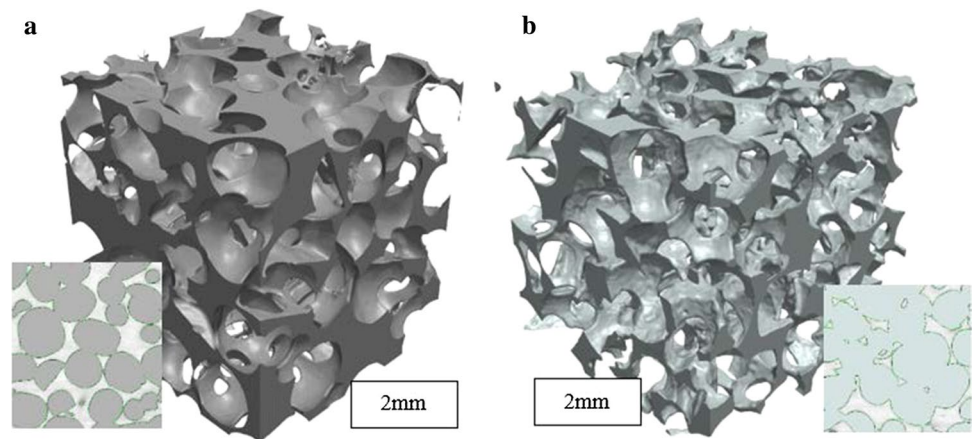
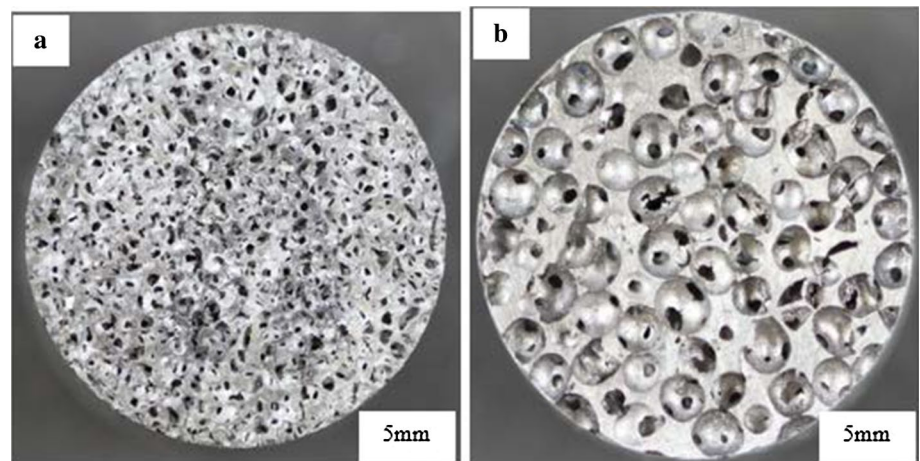


Fig. 6 High resolution 2D optical images of “bottleneck-type” porous aluminium structures made by replication casting processes of applied differential pressure, pore diameter sizes, pore fluid volume fraction and mean pore connectivity of **a** 1 bar, 1.0–1.4 mm, 0.72 and 0.28 mm, **b** 1 bar, 2.5–3.15 mm, 0.75 and 0.72 mm respectively. Sourced from [34]



convergent gap (applied differential pressure, P_i) measured by capillary radius (r_c) Eq. 2.1. The extent to which an applied infiltration pressure, P_i , (used during realistic casting of metal foams) drives liquid metals into the void of packed beds is theoretically considered in [30, 39] to be a function of its capillary radius, r_c , surface tension, σ_{xy} , and wetting angle, θ , (Eq. 2.1) with established wetting data of Al–NaCl available in the literature. Discrete element simulation packings of spherical structures in [38, 39] showed that an inverse power law relation exist between the capillary radius of two connecting virtual spheres and applied differential pressures. In practice, falling permeability measurement of water flow across a 2.0–2.5 mm cell diameter “bottleneck” structure produced at a differential pressure of 1 bar yielded a permeability of $1.28 \pm 0.09 \times 10^{-09} \text{ m}^2$ [30]. Similarly, computational fluid dynamics (CFD) modelling and simulation of pressure drop across the a 2.0–2.5 mm virtual “bottleneck” structures generated at 10 μm capillary radius yielded a mean pore opening of 142 μm and permeability value of $1.09 \times 10^{-09} \text{ m}^2$ [30]. CFD simulation across virtual structures generated at higher capillary radius, typically

between 20 and 80 μm showed a much wider pore openings and decreasing order of permeability value when compared to that generated at 10 μm [28, 34, 40]. This approach involves measuring the liquid driving pressure necessary to balance the Laplace pressure.

$$r_c = \frac{2\sigma_{xy}}{P_i} \cos\theta \quad \text{where} \quad r_w = \sqrt{(r_c + r_p)^2 - r_p^2} - r_c \quad (2.1)$$

A novel approach to the processing of porous metallic structure with multi-component, coated pores developed in [11] could also assist in the controlling of their pore openings. In their work, successful coating or coverage of the porogens (salts) with Cu-coating powder (typically below 100 μm in particle diameter) depends on the unvarying moistening of packed beds of salts. With coated pores, the interconnectivity of the porous material was largely reduced but these openings were increased by a gradual decrease in the degree of powder coverage of the porogens. Figure 7 present images of the uncoated and Cu-powder coated “bottleneck” dominated porous metallic structures and loosely packed porogens used for the casting process.

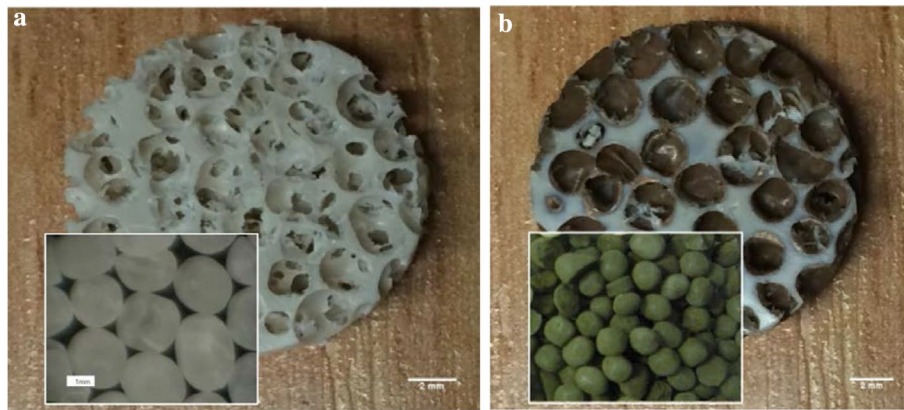


Fig. 7 a Porous structure and loosely packed salt beads and to the right are the b is the porous-coated structure and Cu-coated loosely packed beads. Sourced from [11]

2.7 Space Fillers

The use of water-soluble salts as space fillers is commercially known. Typical examples of these space fillers are sodium chloride (NaCl) and sodium aluminate (NaAlO_2). Numerous advantages like low cost, free of toxicity, and fast dissolution in water are associated with the use of NaCl as favoured space-holder [41]. The sodium chloride (melting point— $800\text{ }^\circ\text{C}$) is a favoured space holder in the replication casting process (RCP) and dissolves rapidly in water while NaAlO_2 is often considered for higher ($1800\text{ }^\circ\text{C}$) melting processes [12]. Precaution should be taken to ensure that complete dissolution of salt in warm water is carried out to avoid limited pore spaces for absorption [4]. Carbamide particles, ammonium bicarbonate particles, magnesium granules, and potassium carbonate particles are also used as fillers. The potassium carbonate particles are used in the lost carbonate sintering (LCS) process because of its high melting ($901\text{ }^\circ\text{C}$) point [8]. One of the advantages of Mg is its low boiling point ($1107\text{ }^\circ\text{C}$) and its complete immiscibility with metals [17]. The high cost of space fillers may deter manufacturers from this process, but regular pore structure and control of pore size give a good foam structure for any engineering application.

3 Fluid Transport in Porous Structures

The part of fluid mechanics that deals primarily with fluid dynamics is termed fluid flow [42, 43]. Fluids are categorized into gases and liquids and when subjected to a motion of unbalanced forces it is called fluid flow. A typical example of this is the flow of water or oil from an overhead tank. The superficial flow velocity (v_s) of the fluid is very high on the top and low at the bottom of the tank with unbalanced

gravitational force (g) enabling a continuous flow of fluid. The defining characteristics of this fluid mirror its properties and how it moves. These properties can be compressible (fractional change in volume due to density variation at different temperature especially for gases) or incompressible (no change in volume especially for water), steady (time-dependent) or unsteady (time-independent), rotational or non-rotational, viscous (shear stress directly proportional to fluid velocity) or non-viscous, Newtonian (viscous stress linearly proportional to local strain rate) or have ability to resist deformation by tensile or shear stress known as a non-Newtonian fluid [36]. The numerical study of this fluid flow is known as computational fluid dynamics (CFD) and is well adopted in the field of science and engineering to mimic flow behaviour even in the paucity of experimental or measured data. The study of fluid flow is governed by the equation of continuity and momentum or Navier–Stokes equation.

3.1 Continuity and Momentum Equations

The generalized form of the continuity equation for fluid flow in the three-dimensional Cartesian coordinate system (typically, in the x , y , and z Cartesian coordinate) reported in [44], is represented Eq. 3.1 for all directions and when considering one direction, Eq. 3.2 holds.

$$\frac{\partial \rho}{\partial t} = -(\nabla \cdot \rho v) \quad (3.1)$$

$$\frac{\partial \rho}{\partial t} + \rho \frac{\partial v_x}{\partial x} = 0 \quad (3.2)$$

where ρ is the fluid density, v is the fluid superficial velocity, $\frac{\partial \rho}{\partial t}$ is the mass change rate with respect to time and $\frac{\partial v_x}{\partial x}$ is the gradient in the unidirectional fluid flow velocity.

Reported in [44], the generalized form of Navier–Stokes equation relates the rate of momentum increase per unit volume as a function of the rate of momentum addition by convection per unit volume $[\nabla \rho \cdot v \cdot v]$, the rate of momentum addition by molecular transport per unit volume $[\nabla p] - [\nabla \tau]$, and external force on fluid per unit volume $[\rho g_i]$ as shown in Eq. 3.3. Also, the shear stress component (τ) in Eq. 3.3 can be expressed in terms of fluid viscosity (μ) and velocity (v) and Eq. 3.4 holds for a constant density (ρ) and viscosity (μ).

$$\frac{\partial}{\partial t} \rho \cdot v = -[\nabla \rho \cdot v \cdot v] - [\nabla p] - [\nabla \tau] + [\rho g_i] \quad (3.3)$$

$$\rho \left(\frac{\partial v}{\partial t} + (v \cdot \nabla)v \right) = -\nabla p + \mu \nabla^2 v + \rho g_i \quad (3.4)$$

The negative sign is an indication that fluid flows in the direction of pressure drop. The non-linear partial differential and time-dependent Eq. 3.4 is often solved using commercial CFD software installed in a computer to find a numerical solution at a finite number of points or mesh or grid or discretization. This equation (Eq. 3.4) described the motion of fluid substances and it arises from the application of Newton's second law of fluid motion with the assumption that the sum of a proportional gradient of velocity (diffusing viscous term) and a pressure term described the stress [45].

$$\rho \left(\frac{\partial v}{\partial t} + v \cdot \nabla v \right) = -\nabla p + \nabla \cdot T + F \quad (3.5)$$

where $-\nabla p$ is the gradient of pressure, v is the fluid velocity, ρ is the fluid density, μ is the fluid dynamic viscosity, p is the pressure, T is the component of total stress tensor with an order two, F is the body force (per unit volume) acting on the fluid and the del operator is represented as ∇ . The equation can be defined for compressible or incompressible flow and for a horizontal flow or against gravitational effect Eq. 3.5 is reduced to Eq. 3.6.

$$\rho \left(\frac{\partial v}{\partial t} + (v \cdot \nabla)v \right) = -\nabla p + \mu \nabla^2 v \quad (3.6)$$

At very low or creeping superficial fluid velocity, the rate of pressure drop in a unit length is linearly proportional to fluid velocity and the Navier–Stokes equation reduces to the Stokes equation and is stated below;

$$\rho \left(\frac{\partial v}{\partial t} + (v \cdot \nabla)v \right) = 0, 0 = -\nabla p + \mu \nabla^2 v + \rho g_i \quad (3.7)$$

Equation 3.7 is often solved computationally when the fluid velocity is relatively small or within Darcy regime of laminar flow of fluid. Also, for inviscid fluids or highly viscous and sticky fluids where shear stress ($[\nabla \cdot \tau] = 0$) or velocity at the surface is zero ($v = 0$), the Euler equation (Eq. 3.8) is solved. Against gravitational effects ($g = 0$), the Navier–Stokes equation reduces to;

$$\rho \left(\frac{\partial v}{\partial t} + (v \cdot \nabla)v \right) = -\nabla p + \rho g_i \quad (3.8)$$

3.2 Pore-Scale and Fluid Models

The modelling of fluids across a porous medium involves solving the Navier–Stokes equation at macroscopic or microscopic level. The treatment of foam as a homogeneous medium by neglecting small-scale details is associated with a volume averaging or macroscopic approach [46]. Conversely, the determination of macroscopic parameters used to depict the dynamic behaviour of fluid flow in porous media based on the micro-geometry (representative volume element) of the system by capturing small-scale details is described as pore-scale or microscopic approach [47]. This microscopic approach is more suitable in describing the macroscopic parameters (permeability, porosity, tortuosity and foam surface area per unit bulk volume) of porous metallic structures because of its ability to capture detailed information of the porous matrix [47–50]. Having knowledge of the fluid properties (fluid density and dynamic viscosity), porosity, porous body layer or thickness one can use the pore-scale numerical approach to describe the fluid flow at various velocities to estimate the pressure drop within the porous body.

The estimated or computed values of pressure drops are used to account for the permeability term of porous structures, and inertial term, in the case of high-velocity flow. Several equations have been developed to mimic the behaviour of fluid in the pore region and are listed below.

- Darcy's Law: Describes low-velocity flows of one or more fluids, where the pressure is the major driving force.
- The Richard's Equation: Governs the wetting and driving of rocks or soil.
- The Fracture Flow is a variant of Darcy's law that defines the flow along the interior boundaries representing fractures within a porous (or solid) medium.
- The Brinkmann equation is for porous media high-velocity flows but in the Laminar region ($1 < Re < 10$).
- The free and porous media flow combines free flow adjacent to the porous domain.
- The Laminar flow and creeping flow use the Navier–Stokes equations to describe free flows within a river or well.

Listed above are often derived from the Navier–Stokes equations governing fluid flow.

3.2.1 Darcy Law

Darcy's law states that the velocity field of fluid flow in a porous medium is determined by the gradient of pressure, the structure of the porous medium (permeability and porosity) and fluid viscosity [51]. The law was put together by Henry Darcy based on series of experimental trials [52]. The net flux across a face of porous surface is mathematically expressed as;

$$v_s = -\frac{k_o}{\mu}(\nabla p + \rho g \nabla D) \quad (3.9)$$

where u , k_o , μ , p , ρ , g and ∇D are the Darcy velocity (or specific discharge vector m/s), permeability of the porous medium (m^2), dynamic viscosity (Pa s), fluid's pressure (Pa), fluid density (kg/m^3), magnitude of gravitational acceleration (m/s^2) and unit vector in the direction over which the gravity acts respectively. In other to turn of the gravity effects, the elevation D in [51] was set to zero and the resulting equation is given in Eq. 3.10. Also, models can define the capacity to transmit flow using hydraulic conductivity (K , m/s) given by Eq. 3.11.

$$v_s = -\frac{k_o}{\mu} * \nabla p \quad \text{where} \quad v_p = v_s / \epsilon \quad (3.10)$$

$$v_s = -\frac{K}{\rho g}(\nabla p + \rho g \nabla D) \quad \text{where} \quad \frac{k_o}{\mu} = -\frac{K}{\rho g} \quad (3.11)$$

The hydraulic conductivity K (m/s) represents both fluid and the solid matrix while the permeability is a property of the porous matrix only. The pressure p can also be expressed in term of the hydraulic head, H , pressure head H_p , and elevation head, D as described in Eq. 3.12. The elevation head, D denotes the direction over which g acts. The hydraulic head is equal to the pressure head only when a gravity effect is insignificant, and D is set to zero. When defined as vertical elevation, the vertical gradient in D equals one and the horizontal gradient in D equals zero. Similarly, the average linear velocity (also termed the seepage velocity) within a given pore space is defined by Eq. 3.11 as a function of the superficial fluid velocity (v_s) and porosity (ϵ) of the porous medium.

$$H_p = \frac{p}{\rho g} = H - D \quad (3.12)$$

In summary, the Henry Darcy's law interface built into commercial CFD packages (COMSOL Multiphysics, Ansys Fluent, and Simpleware) can be used to model single and multiphase flows across porous-related structures and typically in this case, porous metals. The Darcy's law interface combines Darcy's law with continuity equation; it is used to simulate fluid flow through interstices in a

porous medium. It is also used to simulate flow for which pressure gradient is the major driving force and highly influenced by the frictional resistance within the pores. It can also be used to model media where porosity and permeability are very small or low-velocity flow [53].

3.2.2 Brinkmann Equation

The Brinkmann equation is used to compute pressure fields and fluid velocity of single-phase flow in porous media at high velocity in the laminar flow regime. Fluid with varying density of Mach number below 0.3 is included. The fluid viscosity can also vary, for example, to describe non-Newtonian fluids. The Mach number is defined as the ratio of fluid velocity to speed of sound [53]. Fast-moving fluids in porous media with kinetic potential from pressure, gravity and fluid velocity to drive the flow is described using Brinkmann equations. The physics interface in commercial CFD packages uses Darcy's law to describe the dissipation of kinetic energy by viscous shear, similar to Navier–Stokes equations. This physics interface is well suited for transitions from slow flow in porous media described by Darcy's law and fast flow in channels governed by Navier–Stokes equations [54]. The modelling of non-Newtonian fluids, like the flow of oil from a reservoir to a well-perforation, hyperbolic zone near a river can be described by the coupling of Brinkmann and Navier–Stokes also known as Stokes–Brinkmann equation.

The Brinkmann equation of flow in porous media is formed from the combination of the continuity equation and the momentum equation described below:

$$Q_{br} = \frac{\partial}{\partial t}(\rho \epsilon) + \nabla \cdot (\rho v) \quad (3.13)$$

$$\frac{\rho}{\epsilon} \left(\frac{\partial v}{\partial t} + (v \cdot \nabla) \frac{v}{\epsilon} \right) = -\nabla p + \nabla \cdot \left[\frac{1}{\epsilon} \left\{ \mu (\nabla v + (\nabla v)^T) - \frac{2}{3} \mu (\nabla \cdot v) I \right\} \right] - \left(k_o^{-1} \mu + \frac{Q_{br}}{\epsilon^2} \right) v + F \quad (3.14)$$

where μ is the dynamic viscosity of the fluid in $kg/m \ s$; v is the velocity vector in m/s ; ρ is fluid density in kg/m^3 ; p is the pressure measured in Pa ; ϵ is porosity (0–1); k_o is permeability tensor of the porous medium; the mass sink or mass source is Q_{br} measured in $kg/m^3 \ s$; and the force term F ($kg/m^2 \ s^2$) accounts for the influence of gravity and other volume forces. The mass source (Q_{br}), accounts for the mass creation and mass deposit within the domains. Zero velocity is assumed for the mass exchange. It is important to understand that Eq. 3.13 is the continuity expression for a compressible flow. For an incompressible flow with constant density, Eq. 3.13 reduces Eq. 3.15.

$$Q_{br} = \rho \nabla \cdot v \quad (3.15)$$

3.2.3 Boundary Conditions

A boundary condition is a form of an equation or a stated restriction that limits the possible solutions to a differential equation [54]. It is a condition where a differential equation is solved [55]. Setting out the right boundary condition when resolving the fluid models thereof, can help us to differentiate between right and wrong or solve our computation easily. Table 1 presents a summary of most commonly used boundary conditions for application involving fluid flows.

3.3 Darcy–Dupuit–Forchheimer Model

It is important for us to note that Henry Darcy’s empirical model in Eq. 3.10 expresses the volumetric flow rate of fluid flow in porous media as a function of pressure gradient and fluid properties (permeability and fluid viscosity). His expression is valid for fluid flow in the Darcy region of laminar flow and shows a linear relationship between flow rate and pressure drop in a porous medium at very low fluid flow velocity [9, 30, 57]. Experimental studies on flowing gas across packed beds of coal at high velocity performed by Philippe Forchheimer in 1901 observed the non-linearity between the fluid flow rate and the driving pressure gradient. Inertia effects caused by the non-linear increase in turbulence in the fluid flow rate become

significant at this high velocity in the porous medium [58–60]. An inertia effect also known as the Forchheimer term and is added to Darcy’s empirical equation (Eq. 3.10) to account for this non-linearity as shown in Eqs. 3.16–3.18:

$$-\frac{\partial p}{\partial x_i} = \frac{\mu}{k_o} v_s + \rho C v_s^2 \tag{3.16}$$

$$-\frac{\partial p}{\partial x_i} = \nabla P = \frac{\mu}{k_o} v_s + \rho \frac{C_F}{\sqrt{k_o}} v_s^2 \tag{3.17}$$

$$v_s = \frac{A_f}{A_T} v_p = \varepsilon v_p \quad \text{and} \quad \nabla P = \frac{\mu}{k_o} \frac{A_f}{A_T} v_p + \rho \frac{C_F}{\sqrt{k_o}} \left(\frac{A_f}{A_T} v_p \right)^2 \tag{3.18}$$

where k_o is the permeability of the porous medium, A_f is the average pore area, A_T is the total cross-sectional area in a direction of flow (x, y, or z), C is the inertial factor or Form drag coefficient (measured in m^{-1} or ft^{-1}), ρ is the fluid density flowing through the porous medium, C_F is the Ergun’s or Forchheimer coefficient, v_s is the inlet superficial velocity and v_p is the pore or modified inlet velocity based on the porosity of the foam microstructure or void fraction in the case of flow description in packed beds of particle.

Table 1 Summary of common boundary conditions for fluid flow [56]

Boundary	Boundary conditions	Equation	Use
Wall	Sliding wall	$v = v_w$	Used to specify the velocity of a moving wall
	No-slip (default)	$v = 0$	Zero velocity at the wall
Inlet	Velocity	$v = -nv_o$ or $v = v_o$	To specified constant velocity or a defined velocity by an equation as $v = a(1 - (\frac{z}{R})^2)$. Where n is a unit vector normal to the surface
	Pressure, no viscous stress	$p = p_o$ and $\mu(\nabla v + (\nabla v)^T)n$	Use to describe fluid inlet perpendicular to the boundary
Outlet	Velocity	$v = -nv_o$ or $v = v_o$	Be careful not to over-specify
	Pressure, no viscous stress	$p = p_o$ and $\mu(\nabla v + (\nabla v)^T)n$	Used to describe fluid outlet perpendicular to the boundary
Symmetry	Slip/symmetry condition	$v \cdot n = 0$	Used to specify no velocity perpendicular to a surface or an area. For example, fluid flow in a 3D porous object, the inlet and outlet may be velocity or pressure flow while the other sides are treated as symmetry
	Normal flow/pressure or ‘straight-out’ BC	$p = p_o$ & $v \cdot t = 0$	Used for fully developed flow perpendicular to the area
	Outflow/pressure BC	$p = p_o$	Used for known pressure
Periodic	Velocity	$v_{(x0)} = v_{(x1)}$	This typically implements standard periodicity so that, the value of the solution is the same on the periodic boundaries. This isn’t suitable for spherical or elliptical objects but a line, cube and rectangular are the most intuitive and common choice and thus can be applied to the side walls of the objects
	Pressure	$P_{(x0)} = P_{(x1)}$	
Open	Velocity and pressure	$v_{(o)} = v_{(1)}$ $P_{(o)} = P_{(1)}$	Describing boundaries in contact with a large volume of fluid. For the open boundary, fluid can both enter and leave the domain on boundaries whilst it can only access the entrance of the object in case of the closed boundary condition
Closed		$v_{(o)} = 0$ $P_{(o)} = 0$	

Additionally, experimental and computational described in [31, 61–63] noted that deviation from this Darcy's law ($Re > 1$) is caused by either high fluid velocity, molecular, non-Newtonian fluid or ionic effects is termed the non-Darcy flow. Acceleration and deceleration effects on the fluid as it travels through the tortuous flow path of the porous medium can result in higher fluid velocity resulting in inertial losses. Thus, the Forchheimer term accounts for this.

3.4 Pressure Drops and Permeability Estimation in Porous Metals

Estimation of permeability for flow in the Darcy regime is done using Eq. 3.10 by plotting the unit pressure drop (∇p) developed across the porous structures against superficial fluid velocity (v_s). For the Darcy–Forchheimer or non-Darcy regime, the determination of permeability and inertial factors for flow through porous structure, a second-order polynomial is used to fit the pressure–velocity data; this is then compared to the Darcy–Dupuit–Forchheimer model (Eq. 3.16). Figure 8 presents measured pressure drop per unit thickness (Pa m^{-1}) against superficial velocity (m s^{-1}) of air flow through an open-celled (10 and 40 pores per inch) metallic foams for porosities of 92.9 and 93.8% respectively [63]. Using the value of air viscosity of $1.8205 \times 10^{-5} \text{ Ns m}^{-2}$ and air density 1.204 kg m^{-3} at 20°C , the permeability (k_o), Form drag (C) and Forchheimer constant (C_F) computed for the 10 PPI foam using Eq. 3.16 are $3.17 \times 10^{-7} \text{ m}^2$, 87.2 m^{-1} and 0.049 whilst that of the 40 PPI foam are $1.73 \times 10^{-7} \text{ m}^2$, 128.4 m^{-1} and 0.05 indicating a stronger dependence of pressure drops on the microstructural arrangement of the porous material.

The number of pores in a linear inch is termed as pores per inch abbreviated as PPI [63, 64] helps determine the

mean pore size of porous structures and the region of interest needed to account for its permeability and inertial coefficients using pore-level approach. Scanning electron microscopy (SEM), optical images and X-Ray computed tomography [65] are used in the determination of the PPI of porous metallic structures. The 10 PPI structures in Fig. 8 is characterised by having larger pore sizes approximately 2.54 mm per pore while that of the 40 PPI has in approximation 0.64 mm per pore. The 40 PPI offers a higher resistance to airflow than the 10 PPI and could be useful for high impact applications with little or no interest in flow across the porous material. For a given flow regime, the permeability and Form drag is constant, but it varies over different velocities at a given PPI. Though, the selection of a given range of velocities would depend on the foam application and the limitation of the experiment.

Otaru et al. [33] reported the pressure drop behaviour of “bottleneck” dominated porous metallic structures made by replication casting of uncoated near-spherical salts (particle diameter sizes in the ranges of 2.0 and 2.5 mm separated by varying degree of applied differential pressures between 0.25 and 0.9 bars) using measurement and predicting computationally fluid dynamics (CFD) approach. Figure 9 present the measured and predictive pressure drop values and a two-dimensional image of the lowest porosity (70.4%) porous metal studied in [33]. Agreements in the pressure drop data between the two approaches in their work were good. Pressure drop values for these structures were observably higher for structure (Y1) with smallest openings ($640 \mu\text{m}$) and porosity (70.6%) and lowest for structure (Y4) with the highest openings ($920 \mu\text{m}$) and porosity (78.4%). By fitting the pressure drop and velocity in Eq. 3.16, the permeability and Form drag obtained for the lowest and highest pore volume porous metallic structures are $1.34 \times 10^{-8} \text{ m}^2$, 17583 m^{-1} and

Fig. 8 Plots of pressure drop per unit length (Pa m^{-1}) across 10 and 40 PPI porous metallic structures against superficial air inlet velocity (m s^{-1}). Sourced from [61]

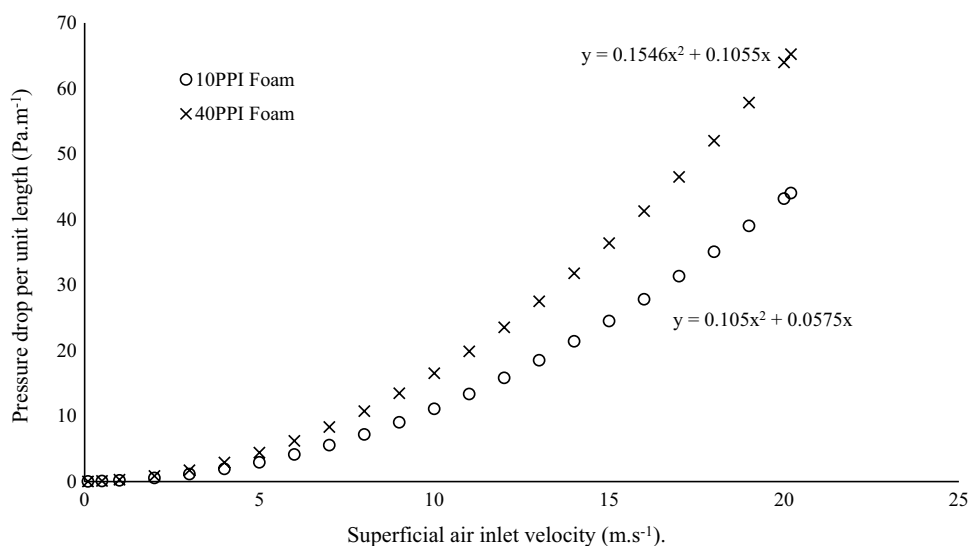


Fig. 9 Measured and CFD predictive pressure drops developed across “bottleneck” dominated porous metallic structures in the Darcy–Forchheimer regime. Adapted from [33]

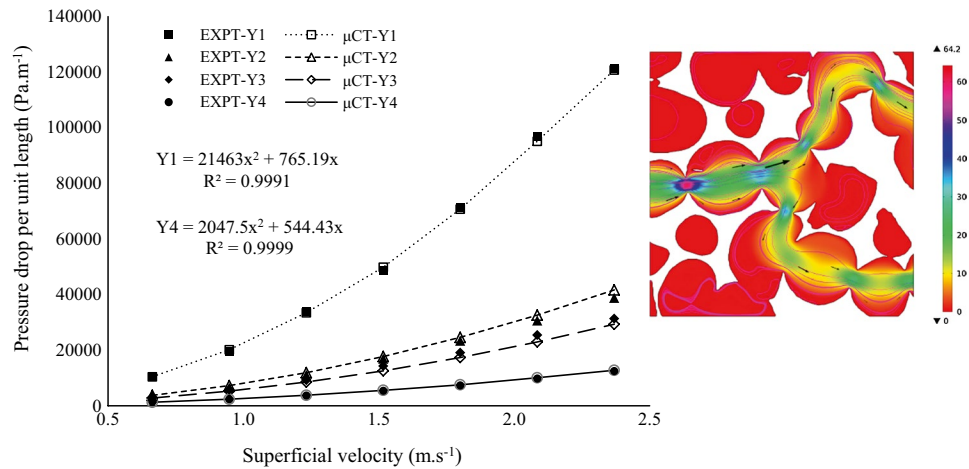
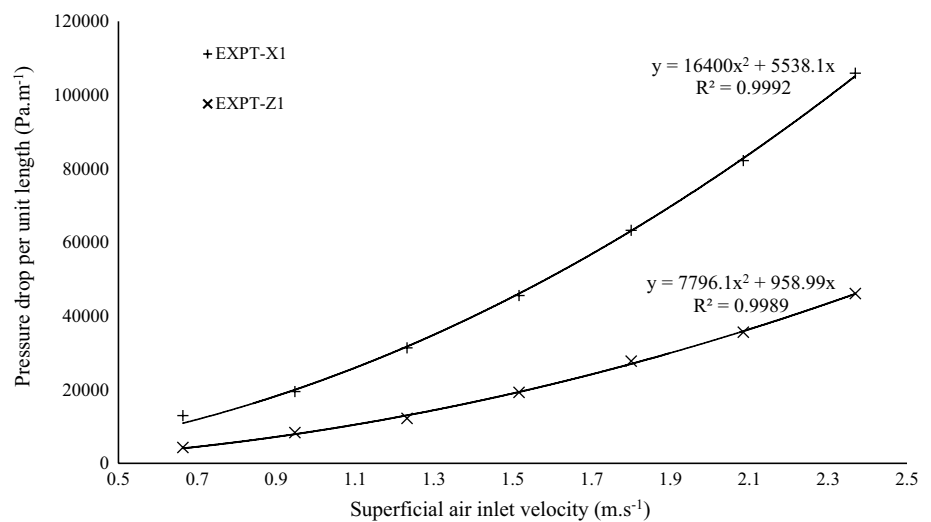


Fig. 10 Plots of measured pressure drop per unit length (Pa m⁻¹) against superficial air inlet velocity (m s⁻¹) six foam structures. Sourced from [34]



$3.35 \times 10^{-8} \text{m}^2$, 1701m^{-1} respectively. This, therefore, highlights the effects imposed by the penetration effects of liquid metals into convergent gaps created by packed beds at high and low applied differential pressures. Relatedly, experimental measurement of pressure drops across “bottleneck-type” porous aluminium structures made by the replication route of similar applied differential (0.9 bars) and different pore diameter sizes (X1/1.0–1.4 mm and Z1/2.5–3.15 mm) reported in [34] are presented in Fig. 10. Expectedly, the unit pressure drops developed across the smaller pore size structure was observably higher than the larger pore size structure. During packings of porogens, the larger beads create a more wider sphere contacts resulting in a much wider pore openings during negative infiltration of liquid melts into the convergent gaps created by the beds thereby lowering the overall structural surface area (specific surface) and unit pressure drops flow developed across the structure.

The “bottleneck-type” porous metals are characterised by larger circular pores and apertures and high surface area. Pressure drop across these structures is expected to be higher

than commercially available porous metallic foams like RecematTM, DuocelTM, PorvairTM and AlantumTM characterised either by transversely isotropic “cell-like” structures or non-uniform sections and extremely larger porosities than the “bottleneck-type” materials. The pressure drop across these highly porous commercially available metal foams can be improved by increasing the surface area of the materials either by compression [66–70] or using the salts coating replication casting techniques described [11]. The permeabilities of the “bottleneck” structures are described in [7, 30, 33, 35, 71, 72] to largely depend on their pore openings (majorly dependent on the applied differential pressures used in the casting method) whilst the Form drag is also reported to depend greatly on the porosity (majorly dependent on the packing density of the porogens) of the materials.

The technological route and operating conditions employed during foam manufacturing process often dictate the topologies of the structures. Generally, the pores in open-celled porous metallic structures relate by touching cells which evidently allows flowing fluids to explore their

internal architecture from the face presented to fluid source to the sample exit. Under mechanical compression of the porous materials, porosity decreases (becoming closed-cells) [63, 67, 70, 73] thereby resulting in increase in the internal surface area (specific surface) and tortuosity of the samples [74]. The increase in tortuosity of the porous materials can be attributed to the increasing pore-nonuniformity of the compressed structures [75] with reduced pore sizes and pore openings. Experimental compression of a 20.5 mm thick Inconel 450 μm highly porous (porosity $\sim 88\%$) to 9.7 mm thick sample in [67] reduces its porosity to 78%. The Forchheimer regime measured permeability of the initial sample decreases from 1.43×10^{-09} to 0.82×10^{-09} m^2 whilst the Forchheimer Form drag coefficient increases from 1.89×10^3 to 18.3×10^3 m^{-1} indicating an increase in the specific surface of the compressed material. Overall, the dependence of permeability and Forchheimer coefficient was observed to linearly depend on the sample porosity for porous metallic structures at varying degree of compression pressures [63, 67, 70, 73].

3.5 Reynolds Number for Flow in Porous Structures

Various authors have used Reynolds number to classify the regime of fluid flow in porous structures. Lage et al. [61], described the pore diameter sized Reynolds number (Re_D) of viscous dominated flow in porous media at very low-velocities to be less than unity ($Re_D < 1.0$) and the behaviour of fluid flow in this regime strongly depends on the morphological features of the porous matrix [57]. Nield and Bejan [46] described the transition of fluid from Darcy to Forchheimer flow regime as smooth and takes place over a range of $1 < Re_D < 10$. The flow in this regime is still laminar but non-linear as inertial forces become imperative and the Darcy–Dupuit–Forchheimer law (Eq. 3.16) holds. The non-linearity deviation from the Darcy regime is caused by inertial effects and not turbulence as the flow is laminar. Turbulence arises at much higher velocities [63]. Boomsma and Poulikakos [76], found out that the departure from Darcy in an open-celled foam took place at $14 < Re_D < 27$ while du Plessis and Wouldberg [77] gave an expression for Reynolds number determination in this regime as a function of open porosity, ϵ (Eq. 3.19). The Forchheimer or form drag dominated, post-Forchheimer unsteady laminar and completely turbulent flow regimes were described in [58], to be within $10 < Re_D < 150$, $150 < Re_D < 300$ and $Re_D > 300$ respectively.

$$Re = \frac{50.8}{C_d} * \frac{(1 - \epsilon)^{\frac{1}{3}}}{\left(1 - (1 - \epsilon)^{\frac{1}{3}}\right)} \quad (3.19)$$

where $C_d = 1.90$ and Re is the Reynolds number ($0 \leq Re \leq 71$ critical Re range) and ϵ is the porosity ($0 \leq \epsilon \leq 1.0$).

The determination of Reynolds number in packed beds has been limited to mean particle or cell diameter, D_p [76–81], as a measure of its characteristic linear dimension (Eq. 3.20) but may differ when used for metal foam structures. From a sequence of experimental data on pressure drops and superficial velocity measured for an open-celled metal foam, Boomsma and Poulikakos [76] and Edouard et al. [82] proffered that the preferred characteristic linear dimension for determination of Reynolds number is its Darcian permeability, k_0 , (Eq. 3.20) as it considers all the macroscopic parameters which best described the geometrical behaviour of the porous matrix. However, the work of Bonnet et al. [83] argued otherwise by using the cell or pore diameter as the preferred characteristic linear dimension for computing Reynolds number (Eq. 3.21) of fluid flow through open-celled metal structures. Equations 3.22 and 3.23 show a Reynolds number description of the Forchheimer model in terms of their permeability-based (Re_k) and pore diameter-based (Re_D) Reynolds numbers. Their corresponding Forchheimer coefficients are represented as C_{FK} and C_{FD} whilst $\nabla p, \mu$ and v_s are the pressure drop per unit thickness, fluid viscosity and superficial fluid velocity respectively.

$$Re_D = \frac{\rho v_s D_p}{\mu} \quad (3.20)$$

$$\frac{\nabla p}{v_s} = \frac{\mu}{k_0} + Re_D \cdot \frac{\mu}{D_p} \cdot \frac{C_{FD}}{\sqrt{k_0}} \quad (3.21)$$

$$Re_K = \frac{\rho \sqrt{k_0} v_s}{\mu} \quad (3.22)$$

$$\frac{\nabla p}{v_s} = \frac{\mu}{k_0} + Re_K \cdot C_{FK} \cdot \frac{\mu}{k_0} \quad (3.23)$$

4 Conclusions

In this survey, diverse routes on the production of metallic foam structures and their fluid flow behaviours have been made known with replication casting process described to be of better economic advantage due to the important and easy control of microstructural properties of metallic structures using this method. It is important to note that nearly all published work on metallic foams focused on the review and application of commercially available high-porous or open-celled (characterized by high porosity ranging between 85 and 95% and low surface area) and close-celled porous metals. This work covers review on processing and fluid flow behaviour of a wide range of porous metallic structures, including the low-porosity or “bottleneck-type” structures

made by the replication casting process. These “bottleneck” structures are characterized by lower porosity ranging between 60 and 75% and higher surface area enabling their usefulness for load-bearing and impact applications.

The fluid section of this review contained within the range of contents including continuity and momentum equation, pore-scale and fluid models, flow regimes, permeability and Form drag estimations. It is to this end that the literature covered herein will assist in the experimental and numerical study of pressure drop across various types of porous metallic structures. Additionally, extensive research work on the discrete element simulation packing of spheres reported in [39] enabled the understanding of the effects imposed by monomodal and bimodal packings on the microstructural changes of bottleneck structures. Whilst flow distribution in bottleneck structures characterised by monomodal pore sizes distribution have been previously studied and reported in [7, 9, 29, 33, 34], this review would enable an insight into a deep understanding on researching the flow behaviour characterised by bimodal structures using experimental and predictive analysis.

Acknowledgements OAJ would like to thank the University of Nottingham Dean of Engineering Research Scholarship for International Excellence for providing me with the needed funds and facilities required for the successful completion of this work. Many thanks to Professor Andrew R. Kennedy (Lancaster University, UK) and Professor Herve P. Morvan (University of Nottingham, UK) for their overwhelming contributions.

Compliance with Ethical Standards

Conflict of interest The author of this work declares that He has no conflict of interest.

References

1. P.A. Jorge, J.C. Malcom, Recent-trends in porous sound-absorbing materials. *Sound Vib.* **44**, 12–17 (2010)
2. B. Koo, Y. Yi, M. Lee, B. Kim, Effect of particle size and forming pressure on pore properties of Fe–Cr–Al porous metal by pressureless sintering. *Met. Mater.* **23**(2), 336–340 (2017)
3. J.H. Jung, V.D. Krstic, H.K. Cho, Numerical analysis of effective thermal conductivity associated with microstructural changes of porous SiC as an inert-matrix. *Met. Mater.* **7**(1), 21–26 (2001)
4. A.R. Kennedy, Porous Metals and Metal Foams Made from Powders, Powder Metal. (2012). <https://doi.org/10.5772/33060>
5. J. Zhou, Porous metallic materials, in *Advanced Structural Materials*, ed. by W.O. Soboyejo (CRC Press, Taylor & Francis Group, Boca Raton, 2006), p. 22
6. M.F. Ashby, L.U. Tianjin, Metal foams: a survey. *Sci. China Ser. (b)* **46**(6), 521–530 (2003)
7. E.L. Furman, A.B. Finkelstein, M.L. Cherny, The permeability of aluminium foams produced by replicated-casting. *Metals* **3**, 49–57 (2013)
8. C.Y. Zhao, Review on thermal transport in high porosity cellular metal foams with open cells. *Int. J. Heat Mass Transf.* **55**, 3618–3632 (2012)
9. A.J. Otaru, H.P. Morvan, A.R. Kennedy, Modelling and optimisation of sound absorption in replicated microcellular metals. *Scripta Mater.* **150**, 152–155 (2018)
10. N. Dukhan, Analysis of Brinkman-extended Darcy flow in porous media and experimental verification using metal foam. *ASME J. Fluids Eng.* **134**(7), 071201 (2012)
11. A.R. Siddiq, A.R. Kennedy, A novel method for the manufacture of porous structures with multi-component, coated pores. *Mater. Lett.* **196**, 324–327 (2017)
12. M.F. Ashby, A. Evans, A.R. Kennedy, The role of oxidation during compaction on the expansion and stability of Al foams made via a PM route. *Adv. Eng. Mater.* **8**, 568–570 (2006)
13. P. Habisreuther, N. Djordjevic, N. Zarzalis, Statistical distribution of residence time and tortuosity of flow through open-cell foams. *Chem. Eng. Sci.* (2009). <https://doi.org/10.1016/j.ces.2009.07.033>
14. N. Dukhan, O. Bagci, M. Ozdemir, Experimental flow in various porous media and reconciliation of Forchheimer and Ergun relation. *Exp. Thermal Fluid Sci.* **57**, 425–433 (2014)
15. P. Ranut, E. Nobile, L. Mancini, High resolution microtomography-based CFD simulation of flow and heat transfer in aluminium metal foams. *Appl. Thermal Eng.* (2013). <https://doi.org/10.1016/j.applthermaleng.2013.11.056>
16. F. Garcia-Moreno, Commercial applications of metal foams: their properties and production. *Materials* **9**, 85 (2016)
17. J. Banhart, Manufacture, characterization, and application of cellular metals and metal foams. *Prog. Mater. Sci.* **46**, 559–632 (2001)
18. B.H. Smith, S. Szyniszewski, J.F. Hajjar, Steel foam for structures: a review of applications, manufacturing and material properties. *J. Constr. Steel* **71**, 1–10 (2012)
19. L.D. Kenny, Mechanical properties of particles stabilized aluminium foam. *Mater. Sci. Forum* **217–222**, 1883–1890 (1996)
20. O. Prakash, H. Sang, J.D. Embury, Structure and properties of AlSiC foam. *Mater. Sci. Eng. A* **199**(2), 195–203 (1995)
21. P. Asholt, in *Metal Foams and Porous Metal Structures*, ed. by J. Banhart, M.F. Ashby, N.A. Fleck (MIT-Verlag, Bremen, 1999), p. 133
22. L. Ma, Z. Song, Cellular structure of aluminium foams during foaming process of aluminium melt. *Scripta Mater.* **39**(11), 1523 (1998)
23. V. Shapovalov, in *Porous and Cellular Materials for Structural Applications*, vol. 521, ed. by D.S. Schwartz et al. (MRS, Warrendale, 1998), p. 281
24. F. Baumgartner, I. Duarte, J. Banhart, Industrialization of powder compact foaming process. *Adv. Eng. Mater.* **2**, 168–174 (2000)
25. V. Gergely, B. Clyne, The FORMGRIP process: foaming of reinforced metals by gas release in precursors. *Adv. Eng. Mater.* **2**, 175–178 (2000)
26. M. Fink, O. Anderson, T. Seidel, A. Schlott, Strongly orthotropic open cell porous metal structures for heat transfer applications. *Metals* **8**, 554 (2018)
27. J. Banhart, Metal foams: production and stability. *Adv. Eng. Mater.* **8**, 781–794 (2006)
28. Y.Y. Zhao, D.A. Sun, A novel sintering dissolution process for manufacturing Al foams. *Scripta Materialia* **44**, 106–110 (2001)
29. M. Bram, C. Stiller, H.P. Buchkremer, D. Stover, H. Bauer, High-porosity titanium, stainless steel and superalloy parts. *Adv. Eng. Mater.* **2**, 196 (2000)
30. A.J. Otaru, A.R. Kennedy, The permeability of virtual macroporous structures generated by sphere-packing models: comparison with analytical models. *Scripta Mater.* **124**, 30–33 (2016)

31. J.E. Rehder, *Manufacturing of Cast Iron with Pre-Reduced Iron Ore Pellets*, United State Patent 44011469 (1983)
32. J. Banhart, J. Baumeister, Deformation characteristics of metal foams. *Mater. Sci.* **33**, 1431–1440 (1998)
33. A.J. Otaru, H.P. Morvan, A.R. Kennedy, Measurement and simulation of pressure drop across replicated microcellular aluminium in the Darcy–Forchheimer regime. *Acta Mater.* **149**, 265–275 (2018)
34. A.J. Otaru, H.P. Morvan, A.R. Kennedy, Airflow measurement across negatively infiltration processed porous aluminium structures. *AIChE J.* (2019). <https://doi.org/10.1002/aic.16523>
35. T.J. Lu, F. Chen, D. He, Sound absorption of cellular metals with semi-open cells. *J. Acoust. Soc. Am.* **108**(4), 1697–1708 (2000)
36. Y. Li, L. Zhendong, F. Han, Airflow resistance and sound absorption behaviour of open-celled aluminium foams with spherical cells. *Proc. Mater. Sci.* **4**, 187–190 (2014)
37. R. Goodall, A. Marmottant, L. Salvo, A. Mortensen, Spherical pore replicated microcellular aluminium: processing and influence on properties. *Mater. Sci. Eng. A* **465**, 124–135 (2007)
38. B.N. Asmar, P.A. Langston, A.J. Matchett, A generalized mixing index in discrete element method simulation of vibrated particulate beds. *Granul. Matter* **4**(3), 129–138 (2002)
39. P. Langston, A.R. Kennedy, Discrete element modelling of the packing of spheres and its application to the structure of porous metals made by infiltration of packed beds of NaCl beads. *Powder Technol.* **268**, 210–218 (2014)
40. A.J. Otaru, *Fluid Flow and Acoustic Absorption in Porous metallic Structures Using Numerical Simulation and Experimentation*, Ph.D. thesis, The University of Nottingham, United Kingdom (2018)
41. Q.Z. Wang, D.M. Lu, C.X. Cui, L.M. Liang, Material science and engineering. *J. Mater. Process. Technol.* **211**, 363 (2011)
42. E. Michael, *The Dawn of Fluid Dynamics: A Discipline Between Science and Technology* (Wiley, Hoboken, 2006), p. ix. ISBN 3-527-40513-5
43. M.A. Rao, *Rheology of Fluid and Semisolid Foods: Principles and Applications*, 2nd edn. (Springer, Berlin, 2007), p. 8. ISBN 978-0-387-70929-1
44. H.K. Versteeg, W. Malasekara, *An Introduction to Computational Fluid Dynamics—The Finite Volume Method*, 2nd edn. (Pearson Education Limited, London, 2007)
45. CMI, Clay Mathematic Institute, Millennium Prize Problem (2014). <https://www.claymath.org/millennium-problems>
46. D.A. Nield, A. Bejan, *Convection in Porous Media*, 2nd edn. (Springer, New York, 1992), pp. 8–91
47. S. Peng, Q. Hu, S. Dultz, M. Zhang, Using x-ray computed tomography pore structure characterization for Berea sandstone: resolution effect. *J. Hydrol.* **472–473**, 254–261 (2012)
48. K.K. Bodla, J.Y. Murthy, S.V. Garimella, Microtomography-based simulation of transport through open-cell metal foams. *Numer. Heat Transf. A Appl.* **7**, 527–544 (2010)
49. G.A. Narsilio, O. Buzzi, S. Fityus, T.S. Yun, D.W. Smith, Upscaling of Navier–Stokes equation in porous media: theoretical, numerical and experimental approach. *Comput. Geotech.* **36**, 1200–1206 (2009)
50. T.P. De Carvalho, H.P. Morvan, D. Hargreaves, H. Oun, A. Kennedy, Pore-scale numerical investigation of pressure drop behaviour across open-cell metal foams. *Transp. Porous Media* **117**(2), 311–336 (2017)
51. S. Whitaker, Flow in porous media I: a theoretical derivation of Darcy’s law. *Transp. Porous Media* **1**, 3–25 (1986)
52. H. Darcy, *Les Fontaines Publiques de la Ville de Dijon* (Dalmont, Paris, 1856)
53. Comsol, *Introduction to the Acoustic Module*, US Patent, 7, 519, 518; 7, 596, 474 and 7, 623, 991 (2015)
54. M. Le Bars, M.G. Worster, Interfacial conditions between a pure and a porous medium: implications for binary alloy solidification. *J. Fluid Mech.* **550**, 151–170 (2006)
55. H. Mifflin, *The American Heritage*[®], (Science Dictionary, 2014)
56. R.P. Hesketh, *Flow Between Parallel Plates-Modified from the COMSOL ChE Library Module* (Department of Chemical Engineering, Rowan University, Glassboro, 2008), pp. 3–4
57. A. Dybbs, R.V. Edwards, A new look at porous media fluid mechanics—Darcy to turbulent, in *Fundamentals of Transport Phenomena in Porous Media. NATO ASI Series (Series E: Applied Sciences)*, vol. 82, ed. by J. Bear, M.Y. Corapcioglu (Springer, Dordrecht, 1984)
58. A. Bejan, *Convection Heat Transfer* (Wiley, Hoboken, 1984)
59. M. Piatek, A. Gancarczyk, M. Iwaniszyn, P.J. Jodlowski, J. Lojewska, A. Kolodziej, Gas-phase flow resistance of metal foams: experiments and modelling. *AIChE J.* **63**(6), 1799–1803 (2017)
60. D. Edouard, M. Lacroix, C. Pham, M. Mbodji, C. Pham-Huu, Experimental measurements and multiphase flow models in solid SiC foam beds. *AIChE J.* **54**(11), 2823–2832 (2008)
61. J.L. Lage, P.S. Krueger, A. Narasimham, Protocol for measuring permeability and form coefficient of porous media. *Phys. Fluids* **17**, 088101 (2005)
62. L. Tadrist, M. Misczevics, O. Rahli, F. Topin, About the use of fibrous materials in compact heat exchangers. *Exp. Thermal Fluid Sci.* **28**, 193–199 (2004)
63. N. Dukhan, *Metal Foams: Fundamental and Applications* (DESTTECH Publication, Inc. Technology and Engineering, Lancaster, 2013), pp. 1–310
64. UAF, Universal Air Filter, (2014). www.uaf.com/frequently_asked_questions
65. N. Dukhan, C.A. Minjeur, A two-permeability approach for assessing flow properties in cellular metals. *J. Porous Mater.* **18**(2), 417–424 (2010)
66. B. Antohe, J.L. Lage, D.C. Price, R.M. Weber, Experimental determination of the permeability and inertial coefficients of mechanically compressed aluminium metal layers. *ASME J. Fluids Eng.* **11**, 404–412 (1997)
67. H. Oun, A.R. Kennedy, Experimental investigation of pressure drop characterization across multilayer porous metal structure. *J. Porous Mater.* **21**, 1133–1141 (2014)
68. O. Reutter, E. Smirnova, J. Sauerhering, S. Angel, T. Fend, R. Pitz-Paal, Characterization of air flow through sintered metal foams. *ASME J. Fluids Eng.* **130**(5), 051201 (2008)
69. N. Dukhan, R. Picón-Feliciano, A.R. Álvarez-Hernández, Air flow through compressed and uncompressed aluminum foam: measurements and correlations. *ASME J. Fluids Eng.* **128**(5), 1004–1012 (2006)
70. J.J. Lu, A. Hess, M.F. Ashby, Sound absorption of metallic foams. *J. Appl. Phys.* **99**, 07511–07519 (1999)
71. J.F. Despois, A. Mortensen, Permeability of open-pore microcellular materials. *Acta Mater.* **53**, 1381–1388 (2005)
72. A.J. Otaru, Enhancing the sound absorption performance of porous metals using tomography images. *Appl. Acoust.* **140**, 183–189 (2019)
73. K. Seah, R. Thampuran, S. Teoh, Parametric studies of the mechanical behaviour of porous titanium. *Met. Mater.* **4**(4), 672–675 (1998)
74. Y.B. Choi, T. Motoyama, K. Matsugi, G. Sasaki, Influence of the specific surface area of a porous nickel to the intermediate compound generated by reaction of a porous nickel and aluminium. *Met. Mater. Int.* **20**(4), 741–745 (2014)
75. Y. Champoux, M.R. Stinson, On acoustical models for sound propagation in rigid frame porous materials and the influence of shape factors. *J. Acoust. Soc. Am.* **92**(2), 1120–1131 (1992)

76. K. Boomsma, D. Poulikakos, The effect of comparison and pore size variations on the liquid flow characteristics in metal foams. *ASME J. Fluids Eng.* **124**, 263–273 (2002)
77. J.P. Du Plessis, S. Wouldberg, Pore-scale derivation of Ergun equation to enhance its adaptability and generalization. *Chem. Eng. Sci.* **63**, 2576–2586 (2008)
78. J.M. Coulson, The flow of fluids through granular beds: effects of particle shape and voids in streamline flow. *Trans. Inst. Chem. Eng.* **27**, 237–257 (1949)
79. M. Muskat, H.G. Botset, Flow of gas through porous materials. *Physics* **1**, 27–47 (1931)
80. S. Ergun, Fluid flow through packed column. *Chem. Eng.* **48**, 89–94 (1952)
81. I. Kececioglu, Y. Jiang, Flow through porous media of packed spheres saturated with water. *ASME J. Fluids Eng.* **116**, 164–170 (1994)
82. D. Edouard, M. Lacroix, C.P. Huu, F. Luck, Pressure drop modelling on solid foam: state-of-the-art correlation. *Chem. Eng. J.* **144**, 299–311 (2008)
83. J.P. Bonnet, F. Topin, L. Tadrist, Flow laws in metal foams: compressibility and pore size effects. *Trans. Porous Media* **73**, 149–163 (2008)

Publisher's Note Springer Nature remains neutral with regard to jurisdictional claims in published maps and institutional affiliations.